

Open Research Online

The Open University's repository of research publications
and other research outputs

Cohesive forces prevent the rotational breakup of rubble-pile asteroid (29075) 1950 DA

Journal Item

How to cite:

Rozitis, Ben; MacLennan, Eric and Emery, Joshua P. (2014). Cohesive forces prevent the rotational breakup of rubble-pile asteroid (29075) 1950 DA. *Nature*, 512(7513), article no. 13632.

For guidance on citations see [FAQs](#).

© 2014 Macmillan Publishers Limited



<https://creativecommons.org/licenses/by-nc-nd/4.0/>

Version: Accepted Manuscript

Link(s) to article on publisher's website:
<http://dx.doi.org/doi:10.1038/nature13632>

Copyright and Moral Rights for the articles on this site are retained by the individual authors and/or other copyright owners. For more information on Open Research Online's data [policy](#) on reuse of materials please consult the policies page.

oro.open.ac.uk

Cohesive forces preventing rotational breakup of rubble pile asteroid (29075) 1950 DA

Ben Rozitis¹, Eric MacLennan¹ & Joshua P. Emery¹

¹Department of Earth and Planetary Sciences, University of Tennessee, Knoxville, TN 37996, US

(brozitis@utk.edu)

Space missions¹ and ground-based observations² have shown that some asteroids are loose collections of rubble rather than solid bodies. The physical behavior of such ‘rubble pile’ asteroids has been traditionally described using only gravitational and frictional forces within a granular material³. Cohesive forces in the form of small van der Waals forces between constituent grains have been recently predicted to be important for small rubble piles (10-kilometer-sized or smaller), and can potentially explain fast rotation rates in the small asteroid population⁴⁻⁶. Hitherto, the strongest evidence came from an analysis of the rotational breakup of main belt comet P/2013 R3 (ref. 7), although that was indirect and poorly constrained by present observations. Here we report that the kilometer-sized asteroid (29075) 1950 DA⁸ is a rubble pile that is rotating faster than that allowed by gravity and friction. We find that cohesive forces are required to prevent surface mass shedding and structural failure, and that the strength of the forces are comparable to, though somewhat less than, that of lunar regolith.

It is possible to infer the existence of cohesive forces within an asteroid by determining if it is a rubble pile with insufficient self-gravity to prevent rotational breakup by centrifugal forces. One of the largest known candidates is near-Earth asteroid 1950 DA (mean diameter of 1.3 km; ref.

8), as it has a rotation period of 2.1216 hr that is just beyond the critical spin limit of ~ 2.2 hr estimated for a cohesionless asteroid⁹. A rubble pile structure and the degree of self-gravity can be determined by a bulk density measurement, which can be acquired through model-to-measurement comparisons of Yarkovsky orbital drift¹⁰. This drift arises on a rotating asteroid with non-zero thermal inertia, and is caused by the delayed thermal emission of absorbed sunlight, which applies a small propulsion force to the asteroid's afternoon side. Thermal-infrared observations can constrain the thermal inertia value¹¹, and precise astrometric position measurements conducted over several years can constrain the degree of Yarkovsky orbital drift². Recently, the orbital semimajor axis of 1950 DA has been observed to be decreasing at a rate of $44.1 \pm 8.5 \text{ m yr}^{-1}$ because of the Yarkovsky effect¹², which indicates that the asteroid's sense of rotation must be retrograde. Using the Advanced Thermophysical Model^{13,14}, in combination with the retrograde radar shape model⁸, archival WISE thermal-infrared data¹⁵ (Extended Data Table 1, and Extended Data Figs 1 and 2), and orbital state¹², we determine the thermal inertia and bulk density of 1950 DA (Methods). The thermal inertia value is found to be remarkably low at $24^{+20}_{-14} \text{ J m}^{-2} \text{ K}^{-1} \text{ s}^{-1/2}$, which gives a corresponding bulk density of $1.7 \pm 0.7 \text{ g cm}^{-3}$ (Fig. 1 and Extended Data Fig. 3). This bulk density is much lower than the minimum value of 3.5 g cm^{-3} required to prevent loss of surface material by centrifugal forces (Fig. 2).

Spectral observations of 1950 DA indicate either an E- or M-type classification in the Tholen taxonomic system¹⁶. However, its low optical albedo and low radar circular polarization ratio⁸ rule out the E-type classification (Extended Data Table 2). The derived bulk density is inconsistent with the traditional view that M-type asteroids are metallic bodies. However, the

Rosetta encounter with main-belt asteroid (21) Lutetia has demonstrated that not all M-type asteroids are metal-rich¹⁷. Indeed, the low radar albedo⁸ of 1950 DA is very similar to that of Lutetia, suggesting a similar composition. The best meteorite analog for Lutetia is an enstatite chondrite¹⁷, which has a grain density of 3.55 g cm^{-3} . Taking the same meteorite analog and grain density for 1950 DA implies a macro-porosity of $51 \pm 19 \%$ and indicates that it is a rubble pile asteroid (Fig. 1).

As the WISE observations were taken when 1950 DA was ~ 1.7 AU from the Sun, the derived thermal inertia value scales to $36^{+30}_{-20} \text{ J m}^{-2} \text{ K}^{-1} \text{ s}^{-1/2}$ at 1 AU because of temperature dependent effects. This scaled value is comparable to that of $\sim 45 \text{ J m}^{-2} \text{ K}^{-1} \text{ s}^{-1/2}$ determined for the lunar surface from thermal-infrared measurements¹⁸, and implies the presence of a similar fine-grained regolith. This is consistent with 1950 DA's low radar circular polarization ratio, which suggests a very smooth surface at centimeter to decimeter scales⁸. The sub-observer latitude of the WISE observations was $\sim 2^\circ$ and indicates that this surface material was primarily detected around 1950 DA's equator.

For the derived bulk density, 1950 DA has $48 \pm 24 \%$ of its surface experiencing negative ambient gravity (Methods) with peak outward accelerations of $(3 \pm 1) \times 10^{-5} g_E$ (where g_E is 9.81 m s^{-2}) around the equator (Figs 1, 2 and 3). This makes the presence of a fine-grained regolith rather unexpected, and requires the existence of cohesive forces in order for 1950 DA to retain such a surface. In granular mechanics, the strength of this cohesive force is represented by the bond number, B , which is defined as the ratio of this force to the grain's weight. Lunar regolith

has been found to be highly cohesive because of van der Waals forces arising between grains¹⁹, and experimental and theoretical studies have shown that the bond number for this cohesive force is given by

$$B = 10^{-5} g_A^{-1} d^{-2} \quad (1)$$

where g_A is the ambient gravity and d is the grain diameter⁵. To prevent loss of surface material requires bond numbers of at least one, but surface stability requires the bond numbers to be greater than ten, which places limits on the possible grain sizes present. For a peak negative ambient gravity of $3 \times 10^{-5} g_E$, this relationship dictates that only grains with diameters less than ~6 cm can be present and stable on the asteroid's surface.

This upper limit of ~6 cm diameter grains is consistent with 1950 DA's lunar-like regolith. In particular, lunar regolith has micron to centimeter sized grains described by an approximate d^3 size distribution^{6,19}. Rubble pile asteroid (25143) Itokawa also has a d^3 grain size distribution but has boulders ranging up to ~40 m in size on the surface²⁰, which is reflected in its much higher thermal inertia value of $\sim 750 \text{ J m}^{-2} \text{ K}^{-1} \text{ s}^{-1/2}$ (ref. 21). 1950 DA might have had large boulders present on its surface in the past, but these would have been progressively lost in order of size as it was spun-up by the YORP effect (i.e. spin state changes caused by the anisotropic reflection and thermal re-emission of sunlight from an irregular shaped asteroid¹⁰). This spinning-up selection process leaves behind the relatively fine-grained regolith with low thermal inertia that we see today⁵, and would work in addition to the thermal fatigue mechanism of asteroid regolith formation²².

To check whether internal cohesive forces are also required to prevent structural failure of 1950 DA, we applied the Drucker-Prager model for determining the failure stresses within a geological material^{4,6} (Methods). In this model, the maximum spin-rate a rubble pile asteroid can adopt depends on its overall shape, degree of self-gravity, and internal strength. The internal strength results from the angle of friction between constituent grains and any cohesive forces present. Utilizing the dynamically-equivalent and equal-volume ellipsoid of 1950 DA, and using an angle of friction typical for lunar regolith of 40° (ref. 19), we find that a minimum cohesive strength of 64^{+12}_{-20} Pa is required to prevent structural failure (Figs 1 and 4). This is less than that of 100 Pa measured for weak lunar regolith¹⁹, and is within the range of 3 to 300 Pa estimated by numerical simulations of rubble pile asteroids⁶. It is also consistent with the range of 40 to 210 Pa estimated for the precursor body of P/2013 R3 (ref. 7). This finding proves that not all small asteroids rotating faster than the cohesionless critical spin limit are coherent bodies or monoliths⁴⁻⁶. It also supports the view that some high-altitude bursting meteors, such as impacting asteroid 2008 TC3 (ref. 23), are very small rubble piles held together by cohesive forces⁶.

Finally, as 1950 DA has a 1 in 4000 chance of impacting the Earth in 2880 (ref. 12), and has the potential to breakup like P/2013 R3 because of its tensional state, it has raised new implications for impact mitigation. Some hypothesized deflection techniques, such as the kinetic impactor²⁴, violently interact with the target asteroid and have the potential to destabilize long-ranging granular force networks present²⁵. With such tenuous cohesive forces holding one of these asteroids together, a very small impulse may result in complete disruption. This may have

happened on the precursor body of P/2013 R3 through a meteorite impact. Therefore, there is a potential danger of turning one Earth threatening asteroid into several if cohesive forces within rubble pile asteroids are not properly understood.

1. Fujiwara, A. *et al.* The rubble-pile asteroid Itokawa as observed by Hayabusa. *Science* **312**, 1330-1334 (2006).
2. Chesley, S. R. *et al.* Orbit and bulk density of the OSIRIS-REx target asteroid (101955) Bennu. *Icarus* **235**, 5-22 (2014).
3. Walsh, K. J., Richardson, D. C. & Michel, P. Spin-up of rubble-pile asteroids: disruption, satellite formation, and equilibrium shapes. *Icarus* **220**, 514-529 (2012).
4. Holsapple, K. A. Spin limits of Solar System bodies: from the small fast-rotators to 2003 EL61. *Icarus* **187**, 500-509 (2007).
5. Scheeres, D. J., Hartzell, C. M., Sánchez, P. & Swift, M. Scaling forces to asteroid surfaces: the role of cohesion. *Icarus* **210**, 968-984 (2010).
6. Sánchez, P. & Scheeres, D. J. The strength of regolith and rubble pile asteroids. *Meteorit. Planet. Sci.* **49**, 788-811 (2014).
7. Hirabayashi, M., Scheeres, D. J., Sánchez, D. P. & Gabriel, T. Constraints on the physical properties of main belt comet P/2013 R3 from its breakup event. *Astrophys. J. Lett.* **789**, L12 (2014).
8. Busch, M. W. *et al.* Physical modeling of near-Earth asteroid (29075) 1950 DA. *Icarus* **190**, 608-621 (2007).
9. Pravec, P. & Harris, A. W. Fast and slow rotation of asteroids. *Icarus* **148**, 12-20 (2000).

10. Bottke, W. F., Vokrouhlický, D., Rubincam, D. P. & Nesvorný, D. The Yarkovsky and YORP effects: implications for asteroid dynamics. *Annu. Rev. Earth Planet. Sci.* **34**, 157-191 (2006).
11. Emery, J. P. *et al.* Thermal infrared observations and thermophysical characterization of OSIRIS-REx target asteroid (101955) Bennu. *Icarus* **234**, 17-35 (2014).
12. Farnocchia, D. & Chesley, S. R. Assessment of the 2880 impact threat from asteroid (29075) 1950 DA. *Icarus* **229**, 321-327 (2014).
13. Rozitis, B. & Green, S. F. Directional characteristics of thermal-infrared beaming from atmosphereless planetary surfaces - a new thermophysical model. *Mon. Not. R. Astron. Soc.* **415**, 2042-2062 (2011).
14. Rozitis, B. & Green, S. F. The influence of rough surface thermal-infrared beaming on the Yarkovsky and YORP effects. *Mon. Not. R. Astron. Soc.* **423**, 367-388 (2012).
15. Mainzer, A. *et al.* NEOWISE observations of near-Earth objects: preliminary results. *Astrophys. J.* **743**, 156 (2011).
16. Rivkin, A. S., Binzel, R. P. & Bus, S. J. Constraining near-Earth object albedos using near-infrared spectroscopy. *Icarus* **175**, 175-180 (2005).
17. Sierks, H. *et al.* Images of asteroid 21 Lutetia: a remnant planetesimal from the early Solar System. *Science* **334**, 487-490 (2011).
18. Wesselink, A. F. Heat conductivity and nature of the lunar surface material. *Bull. Astr. Inst. Neth.* **10**, 351-360 (1948).
19. Mitchell J. K., Houston W. N., Carrier W. D. & Costes N. C. Apollo soil mechanics experiment S-200 final report. *Space Sciences Laboratory Series* 15, issue 7. University of California, Berkeley (1974).

20. Michikami, T. *et al.* Size-frequency statistics of boulders on global surface of asteroid 25143 Itokawa. *Earth Planets Space* **60**, 13-20 (2008).
21. Müller, T. G., Sekiguchi, T., Kaasalainen, M., Abe, M. & Hasegawa, S. Thermal infrared observations of the Hayabusa spacecraft target asteroid 25143 Itokawa. *Astron. Astrophys.* **443**, 347-355 (2005).
22. Delbo, M. *et al.* Thermal fatigue as the origin of regolith on small asteroids. *Nature* **508**, 233-236 (2014).
23. Jenniskens, P. *et al.* The impact and recovery of asteroid 2008 TC3. *Nature* **458**, 485-488 (2009).
24. Ahrens, T. J. & Harris, A. W. Deflection and fragmentation of near-Earth asteroids. *Nature* **360**, 429-433 (1992).
25. Murdoch, N. *et al.* Simulating regoliths in microgravity. *Mon. Not. R. Astron. Soc.* **433**, 506-514 (2013).

Online Content Any additional Methods, Extended Data display items and Source Data are available in the online version of the paper; references unique to these sections appear only in the online paper.

Acknowledgements This publication uses data products from NEOWISE, a project of the Jet Propulsion Laboratory/California Institute of Technology, funded by the Planetary Science Division of NASA. We made use of the NASA/IPAC Infrared Science Archive, which is operated by the Jet Propulsion Laboratory/California Institute of Technology under a contract with NASA.

This work was supported by NASA contract NNM10AA11C (D.S. Lauretta PI) through the New Frontiers program, and by NASA contract NNX12AP32G (J.P. Emery PI) through the Near-Earth Object Observing program.

Author Contributions B.R. performed the thermophysical and cohesive force analyses, E.M. retrieved the WISE data and helped with its analysis, and J.P.E. helped with the scientific interpretation of the results. B.R. wrote the manuscript with all co-authors contributing to its final form.

Author Information Reprints and permissions information is available at www.nature.com/reprints. The authors declare no competing financial interests. Correspondence and requests for materials should be addressed to B.R. (brozitis@utk.edu).

Figure 1: Physical property distributions of (29075) 1950 DA. These were derived by ATPM at the $3\text{-}\sigma$ confidence level by fitting to the WISE thermal-infrared observations and to the observed rate of Yarkovsky orbital drift.

Figure 2: Degree of negative ambient gravity for (29075) 1950 DA. The area of the surface experiencing negative ambient gravity (solid line) is plotted against the primary (left) y-axis, and the peak negative ambient gravity (dashed line) is plotted against the secondary (right) y-axis. Both are plotted as functions of bulk density for the nominal diameter of 1.3 km. The vertical lines represent the $1\text{-}\sigma$ range derived for the bulk density, i.e. $1.7 \pm 0.7 \text{ g cm}^{-3}$.

Figure 3: Gravitational slopes of (29075) 1950 DA. These were produced using the retrograde radar shape model⁸ with the nominal derived bulk density of 1.7 g cm^{-3} . Gravitational slopes greater than 90° , which predominantly occur around the equator, indicate that those surface elements are experiencing negative ambient gravity.

Figure 4: Minimum internal cohesive strength of (29075) 1950 DA. This was calculated using the Drucker-Prager failure criterion as a function of bulk density (x-axis) and angle of friction (legend) for the nominal diameter of 1.3 km. The vertical lines represent the $1-\sigma$ range derived for the bulk density, i.e. $1.7 \pm 0.7 \text{ g cm}^{-3}$.

Methods

Thermophysical modelling

The Advanced Thermophysical Model (or ATPM) was used to determine the thermal inertia and bulk density of (29075) 1950 DA. The ATPM has been developed to interpret thermal-infrared observations of atmosphereless planetary surfaces¹³, and simultaneously make asteroidal Yarkovsky and YORP effect predictions¹⁴. Accurate interpretation of thermal-infrared observations was verified by application to the Moon¹³, and it has been successfully applied to asteroids (1862) Apollo²⁶ and (101955) Bennu² for determining their thermal and physical properties.

To summarize how it works²⁶, the ATPM computes the surface temperature variation for each surface element during a rotation by solving 1D heat conduction with a surface boundary

condition that includes direct and multiple scattered sunlight, shadowing, and re-absorbed thermal radiation from interfacing surface elements (i.e. global self-heating effects). Rough surface thermal-infrared beaming (i.e. thermal re-emission of absorbed solar energy back towards the Sun) is explicitly included in the form of hemispherical craters, which have been shown to accurately recreate the lunar thermal-infrared beaming effect¹³. The degree of roughness for each surface element is specified by a fraction of its area covered by the hemispherical craters, f_R . The asteroid thermal emission as a function of wavelength, rotation phase, and various thermophysical properties is determined by applying the Planck function to the derived temperatures and summing across visible surface elements. The Yarkovsky and YORP effects are then determined by computing the total recoil forces and torques from photons reflected off and thermally emitted from the asteroid surface.

Analysis of WISE thermal-infrared observations

The thermal inertia of 1950 DA was determined using archival WISE thermal-infrared observations, which were obtained on 12-13 July 2010 UT during the WISE All-Sky survey¹⁵. All instances of WISE observations of 1950 DA were taken from the Minor Planet Center database and used to query the WISE All-Sky Single Exposure (L1b) source database via the NASA/IPAC Infrared Service Archive. Search constraints of 10'' within the MPC ephemeris of 1950 DA, and Julian dates within 10 seconds of the reported observations, were used to ensure proper data retrieval. The magnitudes returned from this query were kept only in the instances in which there was a positive object detection or where a 95% confidence brightness upper limit was reported. 1950 DA had a faint apparent visual magnitude of 20.5 when the WISE observations

were taken, and was only detected at $3\text{-}\sigma$ levels or greater in the W3 ($11\text{ }\mu\text{m}$) and W4 ($22\text{ }\mu\text{m}$) channels. Additionally, we only used data points that repeatedly sampled common rotation phases of 1950 DA to ensure consistency, and to avoid outliers, within the data set. This resulted in 14 useable data points in the W3 channel and 2 useable data points in the W4 channel (Extended Data Table 1). The WISE images for these data points were also retrieved to check for any contaminating sources or extended objects surrounding 1950 DA (see Extended Data Fig. 2). The WISE magnitudes were converted to fluxes, and the reported red-blue calibrator discrepancy²⁷ was taken into account. A 5% uncertainty was also added in quadrature to the reported observational uncertainties to take into account additional calibration uncertainties²⁷. As in previous works of WISE asteroid observations (e.g. ref. 15), we color correct the model fluxes using the WISE corrections of ref. 27 rather than color correct the observed fluxes.

The free parameters to be constrained by the WISE observations in the model fitting include the diameter, thermal inertia, surface roughness, and rotation phase. Although the radar circular polarization ratio indicates a very smooth surface at centimeter to decimeter spatial scales⁸, it does not provide a constraint on surface roughness occurring at smaller spatial scales that are comparable to 1950 DA's thermal skin depth ($\sim 1\text{ mm}$). Surface roughness occurring at these spatial scales induce the thermal-infrared beaming effect, which requires that roughness must be left as a free parameter to allow the full range of possible interpretations of the WISE thermal-infrared observations to be obtained. In addition, the uncertainty on 1950 DA's measured rotation period does not allow accurate phasing of the radar shape model between

the light-curve observations taken in 2001 and the WISE observations taken in 2010. Therefore, the rotation phase of the first observation (used as the reference) was left as a free parameter in the model fitting.

In the model fitting, the model thermal flux predictions, $F_{\text{MOD}}(\lambda_n, D, \Gamma, f_R, \varphi)$, were compared with the observations, $F_{\text{OBS}}(\lambda_n)$, and observational errors, $\sigma_{\text{OBS}}(\lambda_n)$, by varying the diameter, thermal inertia, roughness fraction, and rotation phase to give the minimum chi-squared fit

$$\chi^2 = \sum_{n=1}^N \left[\frac{F_{\text{MOD}}(\lambda_n, D, \Gamma, f_R, \varphi) - F_{\text{OBS}}(\lambda_n)}{\sigma_{\text{OBS}}(\lambda_n)} \right]^2 \quad (2)$$

for a set of N observations with wavelength λ_n . Separate thermophysical models were run for thermal inertia values ranging from 0 to $1000 \text{ J m}^{-2} \text{ K}^{-1} \text{ s}^{-1/2}$ in equally spaced steps of $20 \text{ J m}^{-2} \text{ K}^{-1} \text{ s}^{-1/2}$ initially, and then between 0 and $90 \text{ J m}^{-2} \text{ K}^{-1} \text{ s}^{-1/2}$ in $2 \text{ J m}^{-2} \text{ K}^{-1} \text{ s}^{-1/2}$ steps once the likely thermal inertia value had been constrained. The diameter, roughness fraction, and rotation phase were also stepped through their plausible ranges, forming a 4-dimensional grid of model test parameters (or test clones) with the thermal inertia steps. A parameter region bounded by a constant $\Delta\chi^2$ at the $3\text{-}\sigma$ confidence level then defined the range of possible parameters. Finally, counting the number of acceptable test clones in each parameter value bin then allowed the probability distribution for each free parameter to be obtained. The best model fit had a reduced- χ^2 value of 1.06, and an example model fit to the WISE observations is shown in Extended Data Fig. 1.

Unfortunately, the WISE data alone do not place unique constraints on the diameter, thermal inertia, and surface roughness because of its limited phase angle and wavelength coverage. As shown in Extended Data Fig. 3, the best-fitting diameter increases with thermal inertia such that a unique constraint cannot be made. Fortunately, the radar observations had constrained 1950 DA's diameter to be 1.3 km with a maximum error of 10% (ref. 8). Therefore, by allowing the diameter to vary between 1.17 and 1.43 km only, we found that 1950 DA's thermal inertia value must be very low, i.e. $24^{+20}_{-14} \text{ J m}^{-2} \text{ K}^{-1} \text{ s}^{-1/2}$ or $\leq 82 \text{ J m}^{-2} \text{ K}^{-1} \text{ s}^{-1/2}$. This result is consistent with a preliminary upper bound of $110 \text{ J m}^{-2} \text{ K}^{-1} \text{ s}^{-1/2}$ determined by ref. 28 using a simpler thermophysical model that neglected rough surface thermal-infrared beaming effects. In our work, the surface roughness still remains unconstrained, but must be included for the Yarkovsky effect analysis described below. The probability distribution for the derived thermal inertia value is shown in Fig. 1.

Analysis of Yarkovsky orbital drift

The bulk density of 1950 DA could be determined by model-to-measurement comparisons of its Yarkovsky semimajor axis drift. Ref. 12 were able to measure a transverse acceleration of $(-6.70 \pm 1.29) \times 10^{-15} \text{ AU/day}^2$ acting on 1950 DA in its orbit by using optical astrometry dating back to 1950 and radar ranging data taken in 2001 and 2012. This transverse acceleration corresponded to a rate of change in semimajor axis of $(-2.95 \pm 0.57) \times 10^{-4} \text{ AU/Myr}$ or $-44.1 \pm 8.5 \text{ m yr}^{-1}$ (ref. 29). Parameter studies using the ATPM have shown that the Yarkovsky effect is in general enhanced by rough surface thermal-infrared beaming¹⁴. For 1950 DA's oblate shape, fast rotation period, and low thermal inertia, the potential enhancement was rather large (see

Extended Data Fig. 4) and had to be included to prevent underestimation of 1950 DA's bulk density. The overall Yarkovsky drift acting on 1950 DA, $da/dt(D, \Gamma, f_R, \rho)$, for a bulk density ρ was determined from

$$\frac{da}{dt}(D, \Gamma, f_R, \rho) = \left(\frac{D_0}{D} \right) \left(\frac{\rho_0}{\rho} \right) \left[(1 - f_R) \frac{da}{dt}(\Gamma)_{\text{smooth}} + f_R \frac{da}{dt}(\Gamma)_{\text{rough}} + \frac{da}{dt}(\Gamma)_{\text{seasonal}} \right] \quad (3)$$

where $da/dt(\Gamma)_{\text{smooth}}$ is the smooth surface component, $da/dt(\Gamma)_{\text{rough}}$ is the rough surface component, and $da/dt(\Gamma)_{\text{seasonal}}$ is the seasonal component²⁶. Each component was evaluated separately at a specified initial diameter, D_0 , and bulk density, ρ_0 . A Yarkovsky effect prediction was produced for every test clone deemed acceptable from the WISE flux-fitting described above. To produce the distribution of possible bulk densities, each prediction was compared against 500 samples of Yarkovsky drift that were randomly selected from a normal distribution with a mean and standard deviation of $-44.1 \pm 8.5 \text{ m yr}^{-1}$. This ensured that the uncertainty on the measured Yarkovsky drift was taken into account. Extended Data Fig. 3 shows the derived bulk density as a function of thermal inertia for the range of acceptable test clones without a thermal inertia constraint. As indicated, to match the observed drift at the $1-\sigma$ level required the bulk density to be less than 2.7 g cm^{-3} regardless of the thermal inertia value. Using the thermal inertia constraint, the bulk density was constrained to be $1.7 \pm 0.7 \text{ g cm}^{-3}$ and its probability distribution is shown in Fig. 1.

Cohesive force modelling

Surface and internal cohesive forces are required to prevent surface mass shedding and structural failure of 1950 DA, respectively. The surface cohesive forces are proportional to the

magnitude of the negative ambient gravity experienced by the surface. In particular, the gravitational acceleration, \mathbf{g} , acting at a particular point of 1950 DA's surface, \mathbf{x} , was determined using a polyhedral gravity field model³⁰. Under asteroid rotation the ambient gravitational acceleration at that surface point will be modified by centripetal acceleration, such that

$$\mathbf{g}' = \mathbf{g} - \omega^2(\mathbf{x} - (\mathbf{x} \cdot \hat{\mathbf{p}})\hat{\mathbf{p}}) \quad (4)$$

where ω is the asteroid angular velocity and $\hat{\mathbf{p}}$ is the unit vector specifying the orientation of the asteroid rotation pole. The ambient surface gravity, g_A , acting along the surface normal, $\hat{\mathbf{n}}$, of point \mathbf{x} is then given by

$$g_A = -\mathbf{g}' \cdot \hat{\mathbf{n}}, \quad (5)$$

and, finally, the effective gravitational slope, θ , is given by

$$\theta = \cos^{-1}(g_A/|\mathbf{g}'|). \quad (6)$$

To accurately measure the area of its surface experiencing negative ambient gravity each shape model facet was split into one hundred smaller sub-facets. The negative ambient gravity as a function of bulk density is shown in Fig. 2, and a 3D plot of gravitational slope is shown in Fig. 3. The bond number for a particular regolith grain diameter in a specified degree of negative ambient gravity was then determined from equation (1).

The minimum internal cohesive force required to prevent structural failure of 1950 DA was determined analytically from the Drucker-Prager failure criterion and a model of interior stresses within the asteroid^{4,6}. For a homogenous ellipsoidal body with semi-axes a , b , c the average normal stress components are

$$\begin{aligned}
\bar{\sigma}_x &= (\rho\omega^2 - 2\pi\rho^2GA_x)\frac{a^2}{5}, \\
\bar{\sigma}_y &= (\rho\omega^2 - 2\pi\rho^2GA_y)\frac{b^2}{5}, \\
\bar{\sigma}_z &= (-2\pi\rho^2GA_z)\frac{c^2}{5},
\end{aligned} \tag{8}$$

where the A_i terms are dimensionless coefficients that depend only on the shape of the body.

These coefficients are $A_x = 0.57003$, $A_y = 0.60584$, and $A_z = 0.82413$ for the dynamically-equivalent and equal-volume ellipsoid of 1950 DA, which were determined from equation 4.6 of ref. 4. The Drucker-Prager failure criterion using the average stresses is given by

$$\frac{1}{6} \left[(\bar{\sigma}_x - \bar{\sigma}_y)^2 + (\bar{\sigma}_y - \bar{\sigma}_z)^2 + (\bar{\sigma}_z - \bar{\sigma}_x)^2 \right] \leq \left[k - s(\bar{\sigma}_x + \bar{\sigma}_y + \bar{\sigma}_z) \right]^2 \tag{9}$$

where k is the internal cohesion and s is the slope constant. The slope constant is determined from the angle of friction φ using

$$s = \frac{2 \sin \varphi}{\sqrt{3}(3 - \sin \varphi)}. \tag{10}$$

An angle of friction consistent with lunar regolith of 40° (ref. 19) was assumed to calculate the minimum internal cohesive force required to prevent structural failure of 1950 DA using the Drucker-Prager criterion. The minimum internal cohesive force as a function of bulk density for three different angles of friction is shown in Fig. 4.

26. Rozitis, B., Duddy, S. R., Green S. F. & Lowry, S. C. A thermophysical analysis of the (1862) Apollo Yarkovsky and YORP effects. *Astron. Astrophys.* **555**, A20 (2013).

27. Wright, E. L. *et al.* The Wide-field Infrared Survey Explorer (WISE): mission description and initial on-orbit performance. *Astron. J.* **140**, 1868-1881 (2010).
28. Nugent, C. R. Solar radiation and near-Earth asteroids: thermophysical modeling and new measurements of the Yarkovsky effect. *ProQuest, UMI Dissertations Publishing*, 3556842. University of California, Los Angeles (2013).
29. Farnocchia, D. *et al.* Near Earth asteroids with measurable Yarkovsky effect. *Icarus* **224**, 1-13 (2013).
30. Werner, R. A. & Scheeres, D. J. Exterior gravitation of a polyhedron derived and compared with harmonic and mascon gravitation representations of asteroid 4769 Castalia. *Celest. Mech. Dyn. Astron.* **65**, 313-344 (1997).

Extended Data

Extended Data Figure 1: Example ATPM fit to the WISE thermal-infrared observations. This fit (lines) was made for a thermal inertia of $24 \text{ J m}^{-2} \text{ K}^{-1} \text{ s}^{-1/2}$ and a surface roughness of 50%. The error bars correspond to the $1\text{-}\sigma$ uncertainties on the measured data points.

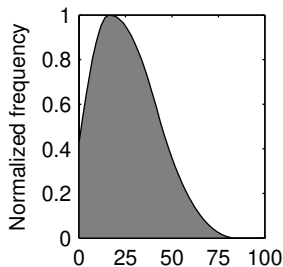
Extended Data Figure 2: WISE thermal-infrared images of (29075) 1950 DA. The image scale is 2.75 arcsec per pixel for the W1/W2/W3 channels and 5.53 arcsec per pixel for the W4 channel. White pixels are bad pixels that do not contain data. The object seen to the upper left of 1950 DA in the W1 and W2 channels is a faint background star.

Extended Data Figure 3: Physical properties derived for (29075) 1950 DA as a function of thermal inertia. **a**, Diameter; **b**, bulk density. The dashed lines represent the 1- σ uncertainty for the average solid lines. The red horizontal lines represent the radar diameter constraint⁸ of 1.30 ± 0.13 km, and the red vertical lines represent the corresponding thermal inertia constraint of $\leq 82 \text{ J m}^{-2} \text{ K}^{-1} \text{ s}^{-1/2}$.

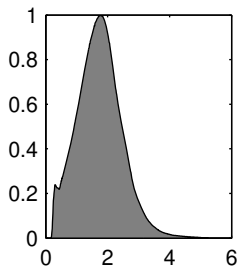
Extended Data Figure 4: Enhancement of Yarkovsky orbital drift by surface roughness for (29075) 1950 DA.

Extended Data Table 1: WISE thermal-infrared observations of (29075) 1950 DA.

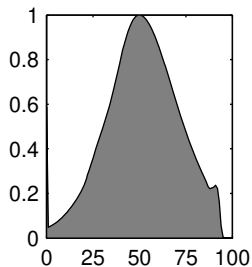
Extended Data Table 2: Physical properties of (29075) 1950 DA. *Derived in this work.



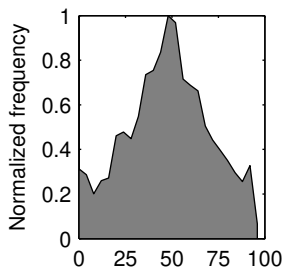
Thermal inertia ($\text{J m}^{-2} \text{K}^{-1} \text{s}^{-1/2}$)



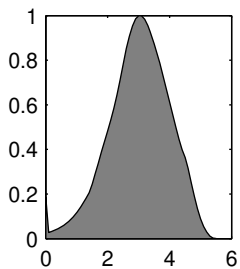
Bulk density (g cm^{-3})



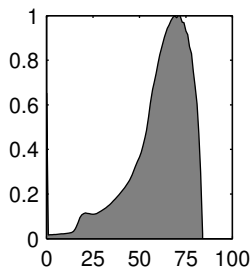
Macro-porosity (%)



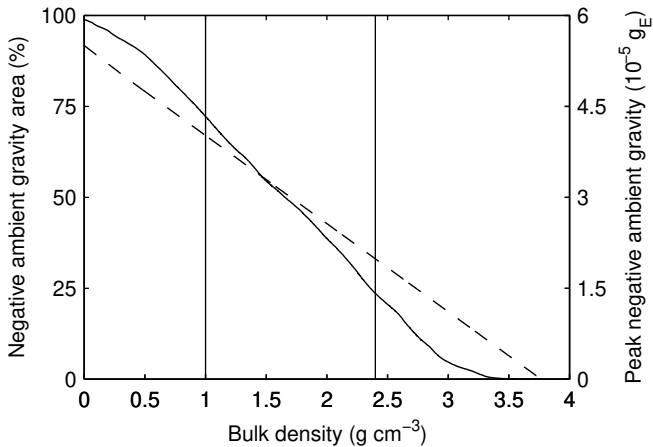
Neg. ambient g. area (%)



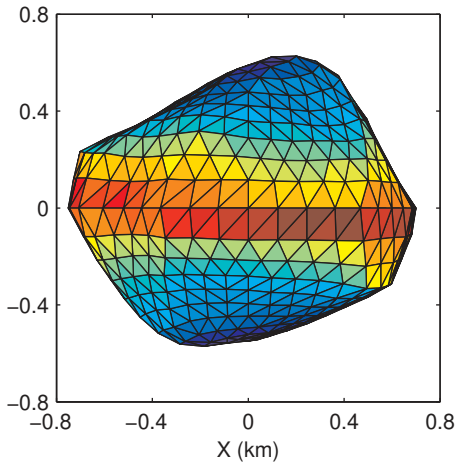
Neg. ambient g. ($10^{-5} g_e$)



Cohesive strength (Pa)



Z (km)



150

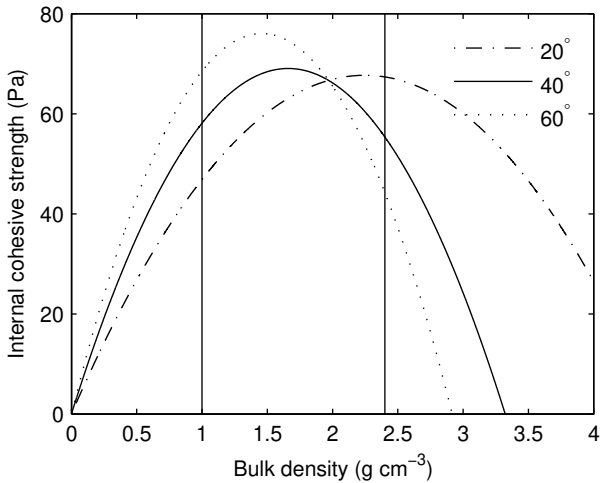
120

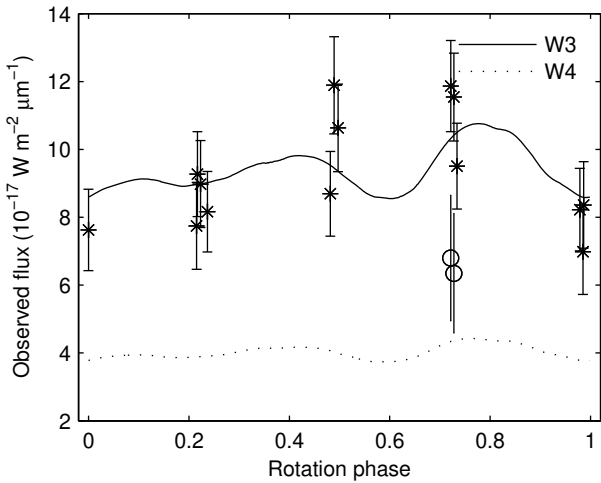
90

60

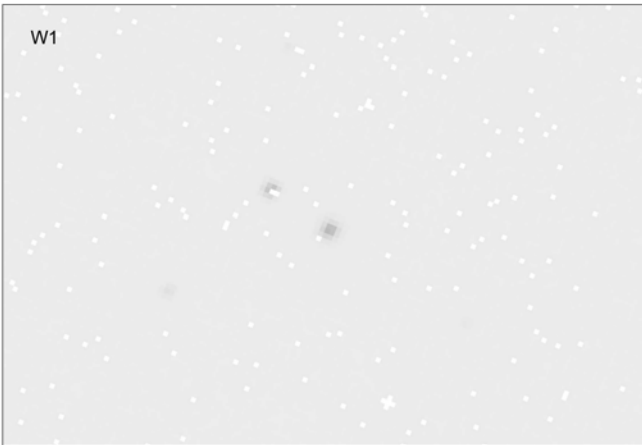
30

Gravitational slope (degrees)

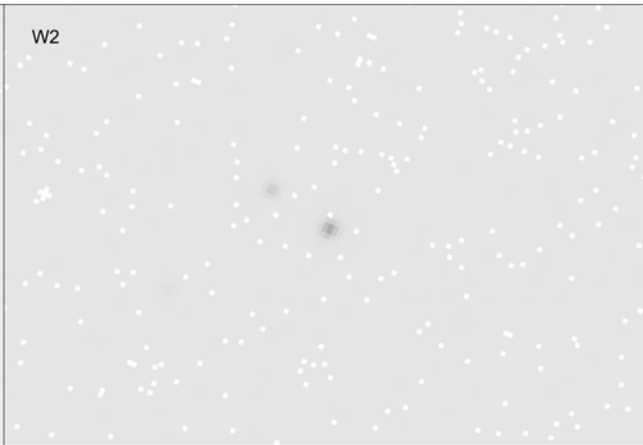




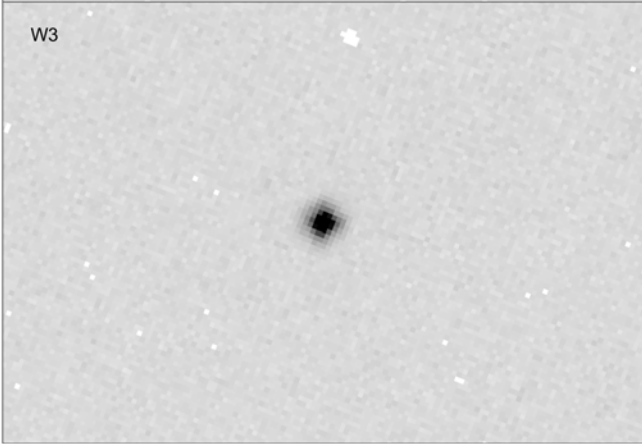
W1



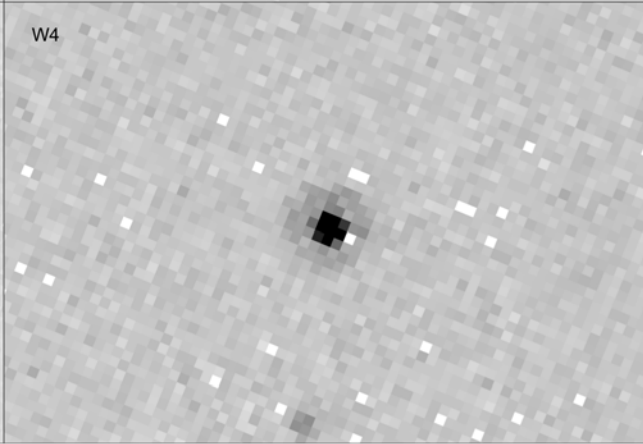
W2

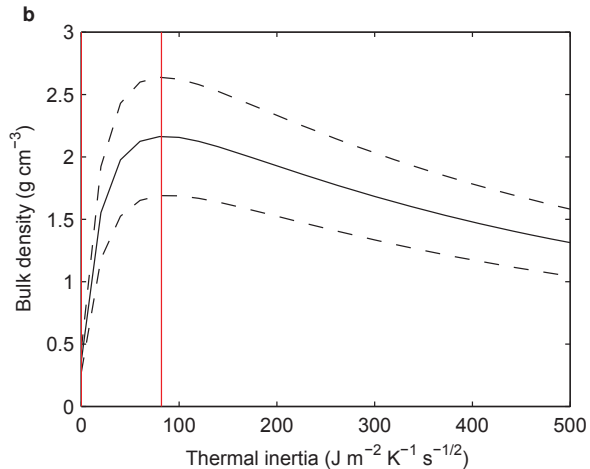
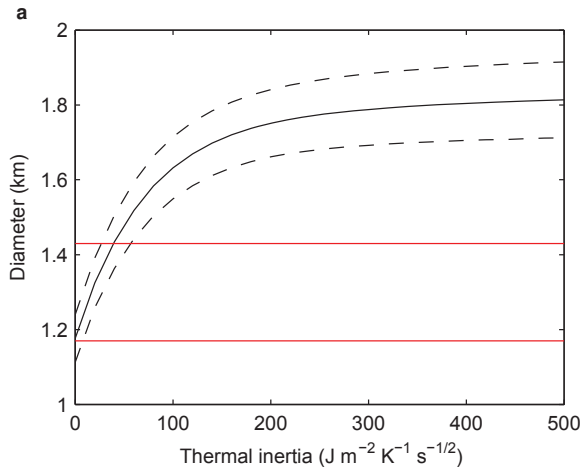


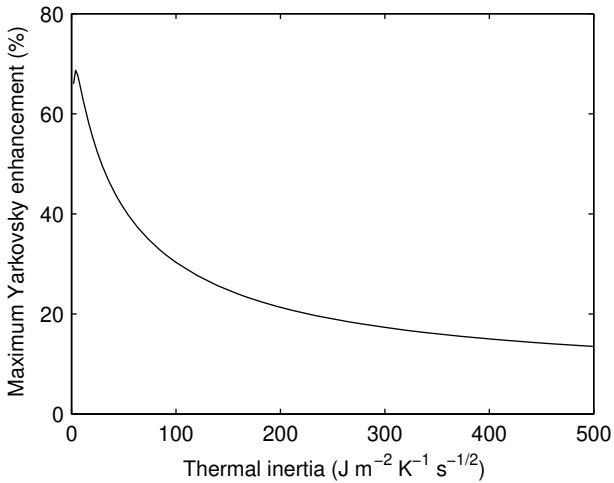
W3



W4







MJD (day)	Rotation phase	Channel	WISE magnitude	Flux (10^{-17} $\text{W m}^{-2} \mu\text{m}^{-1}$)	Heliocentric distance (AU)	WISE-centric distance (AU)	Phase angle (°)
55389.71982	0.000	W3	10.00 ± 0.16	7.63 ± 1.20	1.738	1.410	35.8
55389.85212	0.497	W3	9.64 ± 0.12	10.64 ± 1.29	1.739	1.409	35.8
55390.11670	0.490	W3	9.52 ± 0.12	11.89 ± 1.43	1.741	1.408	35.7
55390.18282	0.238	W3	9.93 ± 0.15	8.17 ± 1.19	1.741	1.407	35.7
55390.24890	0.985	W3	10.10 ± 0.19	6.98 ± 1.26	1.741	1.407	35.7
55390.24903	0.987	W3	9.90 ± 0.16	8.36 ± 1.27	1.741	1.407	35.7
55390.31510	0.734	W3	9.76 ± 0.13	9.51 ± 1.27	1.742	1.407	35.7
55390.38121	0.482	W3	9.86 ± 0.15	8.69 ± 1.25	1.742	1.406	35.7
55390.51351	0.978	W3	9.92 ± 0.15	8.23 ± 1.22	1.743	1.406	35.7
55390.57973	0.727	W3	9.55 ± 0.11	11.54 ± 1.30	1.744	1.405	35.7
55390.71200	0.224	W3	9.82 ± 0.15	8.98 ± 1.28	1.745	1.405	35.6
55390.84433	0.721	W3	9.52 ± 0.11	11.87 ± 1.34	1.745	1.404	35.6
55390.97650	0.216	W3	9.98 ± 0.17	7.75 ± 1.28	1.746	1.403	35.6
55390.97660	0.217	W3	9.79 ± 0.14	9.27 ± 1.25	1.746	1.403	35.6
55390.57973	0.727	W4	7.16 ± 0.30	6.35 ± 1.76	1.744	1.405	35.7
55390.84433	0.721	W4	7.09 ± 0.29	6.80 ± 1.85	1.745	1.404	35.6

	Property	Value
Size	Diameter of equivalent volume sphere ⁸	1.30 ± 0.13 km
	Dimensions of dynamically-equivalent and equal-volume ellipsoid (2 <i>a</i> , 2 <i>b</i> , 2 <i>c</i>) ⁸	1.46 × 1.39 × 1.07 km
Optical	Absolute magnitude ⁸	16.8 ± 0.2
	Phase parameter ⁸	0.15 ± 0.10
	Geometric albedo ⁸	0.20 ± 0.05
Rotation	Rotation period ⁸	2.12160 ± 0.00004 hr
	Obliquity ⁸	168 ± 5 °
Orbit	Semimajor axis ¹²	1.70 AU
	Eccentricity ¹²	0.51
	Yarkovsky semimajor axis drift ¹²	(-2.95 ± 0.57) × 10 ⁻⁴ AU/Myr (or -44.1 ± 8.5 m yr ⁻¹)
Surface composition	Spectral type ¹⁶	M
	Thermal inertia*	24 ^{+20/-14} J m ⁻² K ⁻¹ s ^{-1/2} (36 ^{+30/-20} J m ⁻² K ⁻¹ s ^{-1/2} at 1 AU)
	Surface roughness*	50 ± 30 %
	Radar albedo ⁸	0.23 ± 0.05
	Radar circular polarization ratio ⁸	0.14 ± 0.03
Mass	Bulk density*	1.7 ± 0.7 g cm ⁻³
	Macro-porosity*	51 ± 19 %
	Mass*	(2.1 ± 1.1) × 10 ¹² kg
Cohesion	Surface area of negative ambient gravity*	48 ± 24 %
	Peak negative ambient gravity*	(3 ± 1) × 10 ⁻⁵ g _E
	Internal cohesive strength*	64 ^{+12/-20} Pa